

DarkDiff: Advancing Low-Light Raw Enhancement by Retasking Diffusion Models for Camera ISP

Amber Yijia Zheng^{1*} Yu Zhang² Jun Hu² Raymond A. Yeh^{1†} Chen Chen^{2†}
¹Department of Computer Science, Purdue University ²Apple Inc.

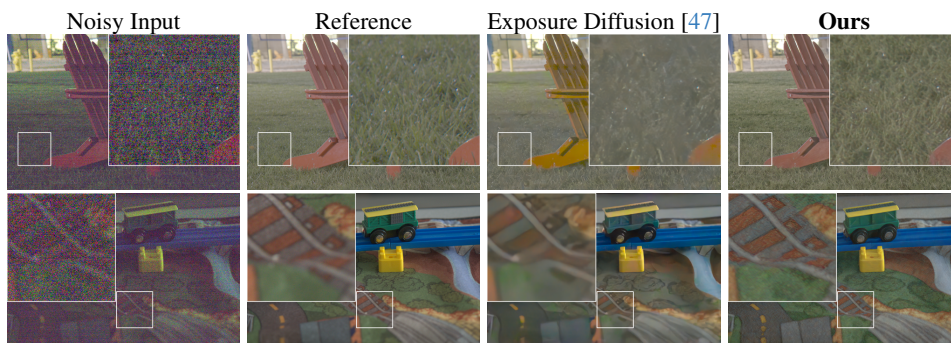


Figure 1: Comparisons of low-light raw image enhancement results. The two input raw images were captured at night with only 0.1s and 0.033s exposure time by a Sony A7SII camera [5]. A digital gain of 300 and gamma correction have been applied for visualization. With sharp and vivid content, our results are comparable to the reference images captured with 300 times longer exposure on a tripod.

Abstract

High-quality photography in extreme low-light conditions is challenging but impactful for digital cameras. With advanced computing hardware, traditional camera image signal processor (ISP) algorithms are gradually being replaced by efficient deep networks that enhance noisy raw images more intelligently. However, existing regression-based models often minimize pixel errors and result in oversmoothing of low-light photos or deep shadows. Recent work has attempted to address this limitation by training a diffusion model from scratch, yet those models still struggle to recover sharp image details and accurate colors. We introduce a novel framework to enhance low-light raw images by retasking pre-trained generative diffusion models with the camera ISP. Extensive experiments demonstrate that our method outperforms the state-of-the-art in perceptual quality across three challenging low-light raw image benchmarks.

1 Introduction

Enhancing noisy *raw* images to vivid, clean sRGB images is typically managed by camera image signal processor (ISP) algorithms in digital cameras, which include image denoising, demosaicing, white balance, color correction, gamma correction, and tone mapping, *etc.*, have become increasingly sophisticated over decades of development [17, 33]. However, capturing images in extremely low-light conditions, where sensor photon count is very low, remains challenging for existing ISP algorithms. When these algorithms fail to recover details from highly noisy areas, oversmoothing or oil-painting appearances are common artifacts.

*Work was done during an internship at Apple Inc.

†Equal advising.

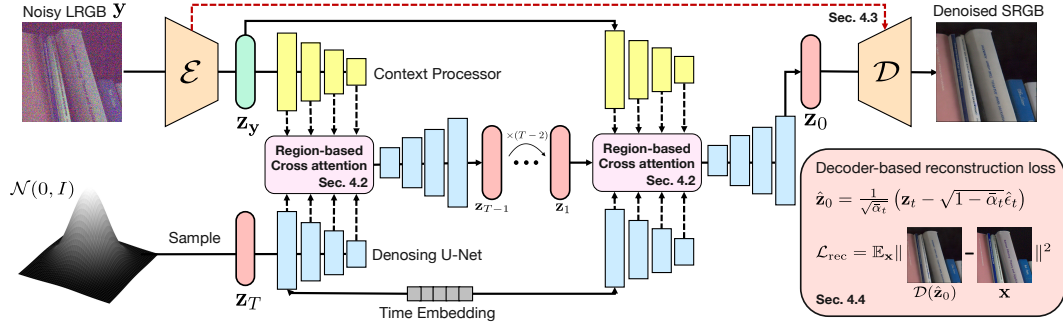


Figure 2: **Overview of the proposed DarkDiff pipeline.** The noisy linear RGB (LRGB) image y is processed by the encoder \mathcal{E} to generate latent representations z_y . These representations and the Gaussian noise are fed into the Denoising U-Net, which integrates a region-based cross-attention between the noisy image and context from the pre-trained model to refine the latent variables z_t . The decoder \mathcal{D} reconstructs the final clean SRGB image x . The region-based cross-attention mechanism (Sec. 4.2) allows the model to leverage contextual information at each denoising step for better detail preservation and noise reduction.

To improve traditional ISP algorithms, existing works mainly focused on regression-based deep networks to enhance the raw images [5, 27, 47]. Seminal work SID [5] collected a dataset of paired noisy raw and clean sRGB images to learn the camera ISP using deep networks, while other works [1, 3, 49, 54] studied different synthetic noise models to improve noise reduction in ISP.

Despite the progress, regression-based methods often encounter the problem of "regression toward the mean," which results in oversmoothed images. To mitigate this, recent work, such as ExposureDiffusion [47], has shifted toward a generative approach to generate *plausible* content in areas with a large amount of noise. However, when image capturing conditions are extreme, ExposureDiffusion [47] still struggles to recover high-resolution image details and accurate colors; see Fig. 1 for examples.

In this work, we leverage the pre-trained StableDiffusion’s [39] generative capability to improve extremely low-light raw image enhancement. A new framework is carefully designed to overcome the limitations of existing deep network-based ISPs. The relatively mature functions in ISP, such as Bayer processing and white balance, are applied before the network. The proposed method learns to map noisy linear RGB images to vivid and clean sRGB outputs. An overview of the method is illustrated in Fig. 2.

We conduct experiments on three challenging datasets, including SID [5], ELD [49], and LRD [54] for extreme low-light raw image enhancement. Results show that our approach outperforms the state-of-the-art (SOTA) in terms of overall perceptual quality (LPIPS [56]) while achieving competitive performance in reconstruction fidelity (measured in PSNR). Additionally, qualitative results show that our approach produces visually more appealing images while preserving high fidelity.

Our contributions are as follows:

- We introduce DarkDiff, a novel approach to retask a pre-trained diffusion model into the camera ISP. Our approach adapts the generative capability trained from large-scale internet images into low-light raw image enhancement, where no large-scale raw datasets are available.
- With a novel architecture design for low-light raw image enhancement, DarkDiff incorporates three key components to effectively address over-smoothing, low fidelity, and color shifts, which are common in prior methods.
- Comprehensive experiments demonstrate that DarkDiff achieves SOTA performance, outperforming baselines in the perceptual metric LPIPS and producing visually higher quality images.

2 Related Work

Low-light image enhancement. One line of research studies the direct enhancement of sRGB images [15, 16, 35, 46, 52, 53], *i.e.*, the output of the camera’s Image Signal Processor (ISP). These works aim to map a low-light dark sRGB image to a properly exposed image under the assumption

that the input images' noise was already addressed by the camera ISP. However, when the ISP does not fully remove the noise, the noise is easily amplified during the enhancement process.

To mitigate this noise implication, another line of work [5, 47, 49, 54] enhances the image at its source, before being fully processed by ISP, *i.e.*, the camera raw data. These methods train end-to-end networks for raw-to-raw or raw-to-sRGB mapping. For instance, SID [5] learns a U-Net with a regression loss on paired noisy raw images and clean sRGB images. ELD [49] and LRD [54] introduce noise models to reduce the domain gap between synthetic and real images, while DNF [26] proposes a two-stage approach that sequentially performs denoising and color correction. However, these methods struggle in regions with extremely low SNR, where input data lacks sufficient information.

Recent works consider generative models to further improve image quality, *e.g.*, using diffusion models [18, 23–25, 37, 47, 53]. At a high level, these methods train diffusion models from scratch using small-scale paired low-light image datasets, which have very limited content generation capability under severe noise conditions. Closely related to our work, LDM-ISP [50] introduces DWT preprocessing and taming modules for low-light enhancement. Differently, we carefully designed the data pipeline to reduce the domain gap and introduced new conditioning modules to better utilize a pre-trained diffusion model.

Image restoration with diffusion. Diffusion models [22, 41, 43, 44] have been used in image restoration [12, 34, 38, 45, 51]. There are also zero-shot methods [11, 29, 36, 45] that utilize the generative power of pre-trained models such as Stable Diffusion [39] without further training. A more comprehensive survey can be found in [19]. Those methods achieved great success by leveraging diffusion generative models trained from large-scale sRGB data. However, there is no raw image dataset at a similar scale. And the way to bridge the domain gap between raw and sRGB is unknown for those diffusion models. Naively using the noisy image as the conditional image in a pre-trained Latent Diffusion Model does not preserve the image content, as shown in Fig. 3.

Cross-attention modules. Cross-attention module [6] was initially designed to compute attention between different token sequences. This idea has been extended to multi-modal tasks, *e.g.*, cross-attention is used to align text and image features to improve text-conditioned image-to-image tasks [7, 20]. In image restoration, cross-attention modules were used to provide conditional input, *e.g.*, Wang et al. [48] uses a cross-attention where the corrupted face image is the query, the high-quality image is the key, and the value is the restored face image. Dang et al. [9] proposed cross-attention between local & global features for low-light image enhancement in sRGB space. In contrast, our proposed region-based cross-attention method preserves local information by grouping tokens.

3 Preliminary

Latent diffusion models. Diffusion models aim to learn a data distribution that is easy to sample from. To make diffusion models more efficient, Latent Diffusion Models (LDMs) [39] use a Variational Autoencoder (VAE) that transforms the data into a latent space, then models diffusion in this space.

LDM begins by passing an input x_0 through the encoder \mathcal{E} , to obtain latent representations \mathbf{z}_0 . The *forward diffusion process* gradually corrupts \mathbf{z}_0 with additive Gaussian noise using the following Markov Chain: $q(\mathbf{z}_t|\mathbf{z}_{t-1}) = \mathcal{N}(\mathbf{z}_t; \sqrt{\alpha_t}\mathbf{z}_{t-1}, (1 - \alpha_t)\mathbf{I})$, where α_t is the noise schedule and t is the timestep. The *reverse diffusion process* learns a denoising network ϵ_θ to undo the added noise. LDM minimizes

$$\mathcal{L}_{\text{LDM}} = \mathbb{E}_{\mathcal{E}(x), t, \epsilon \sim \mathcal{N}(0, \mathbf{I})} [w_t \|\epsilon_\theta(\mathbf{z}_t, t) - \mathbf{n}\|_2^2], \quad (1)$$

where w_t is a weighting factor and $\mathbf{n} \sim \mathcal{N}(0, \mathbf{I})$ is a noise sampled from standard Gaussian.

With a trained ϵ_θ , LDM performs sampling directly in the latent space. Starting from a pure Gaussian noise sample $\tilde{\mathbf{z}}_T \sim \mathcal{N}(0, \mathbf{I})$, LDM iteratively denoise this sample

$$\tilde{\mathbf{z}}_{t-1} = \frac{1}{\sqrt{\alpha_t}} \left(\tilde{\mathbf{z}}_t - \frac{1 - \alpha_t}{\sqrt{1 - \alpha_t}} \epsilon_\theta(\tilde{\mathbf{z}}_t, t) \right) + \sigma_t \mathbf{n}, \quad (2)$$

where $\mathbf{n} \sim \mathcal{N}(0, \mathbf{I})$. Finally, the decoder \mathcal{D} maps $\tilde{\mathbf{z}}_0$ back to the input space, producing a generated sample \tilde{x}_0 .

Cross-attention in LDMs. The backbone of LDM's ϵ_θ follows a standard U-Net [40]. To take in the additional input or conditioning \mathbf{c} , LDM introduces a cross-attention layer to align features from U-Net with the conditioning vector \mathbf{c} .

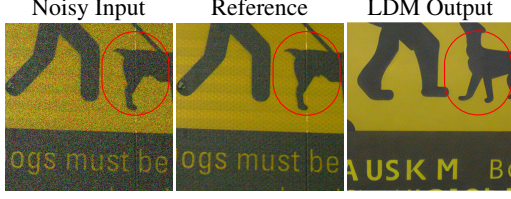


Figure 3: Naively using the noisy image as the conditional image in LDM fails to preserve local structures and leads to hallucinations.

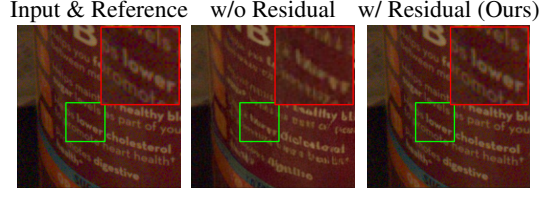


Figure 4: VAE reconstruction results with and without our proposed residual architecture. We observe a loss in input details when not using a residual connection.

Given the latent features (tokens) $\mathbf{z}_t^l \in \mathbb{R}^{N \times d}$ at the l -th layer of U-Net and the condition $\mathbf{c} \in \mathbb{R}^{M \times d}$, a cross-attention computes the queries, keys, and values as follows:

$$\mathbf{Q}^l = \mathbf{z}_t^l (\mathbf{W}_Q^l)^\top, \quad \mathbf{K}^l = \mathbf{c} (\mathbf{W}_K^l)^\top, \quad \mathbf{V}^l = \mathbf{c} (\mathbf{W}_V^l)^\top, \quad (3)$$

where $\mathbf{W}_Q^l, \mathbf{W}_K^l, \mathbf{W}_V^l \in \mathbb{R}^{d \times d_k^l}$ are learned projection matrices for each layer l , and d_k^l is the dimensionality of the attention space. Then the latent features \mathbf{z}_t^{l+1} are updated by

$$\mathbf{z}_t^{l+1} = \mathbf{A}^l \mathbf{V}^l, \text{ where } \mathbf{A}^l = \text{Softmax} \left(\mathbf{Q}^l (\mathbf{K}^l)^\top / \sqrt{d_k^l} \right). \quad (4)$$

Standard cross-attention provides a global receptive field of the entire image, which does not preserve the local structures of the conditioning image.

4 Approach

The task of low-light raw image enhancement is to reconstruct the clean image \mathbf{x}_0 given its noisy observation \mathbf{y} at *raw* domain. This is an ill-posed problem that can be formulated as modeling a conditional probability distribution $p_\theta(\mathbf{x}_0|\mathbf{y})$ using a diffusion model. Instead of training from scratch, our method leverages the generative capability of a pre-trained diffusion model and retasks it to the low-light enhancement task. We proposed a new framework with the following components to achieve the goal:

- *Customized diffusion raw image enhancement pipeline* (Sec. 4.1). We designed a customized pipeline to leverage diffusion models in camera ISP. The raw images are first converted into linear RGB images using standard ISP algorithms to significantly reduce the domain gap with sRGB images.
- *Region-based cross-attention for conditioning* (Sec. 4.2). Naive conditioning in LDM preserves image style but not local structure. As shown in Fig. 3, standard cross-attention leads to structure hallucinations with image content changed. To address this, we propose a region-based cross-attention which helps to align the local details from the noisy observation \mathbf{y} .
- *Content preservation VAE with residuals* (Sec. 4.3). While region-based cross-attention improves the local structure, we need finer control to preserve image content identity, such as text, human faces. To address this, we propose to improve pixel-level fidelity via a residual VAE.
- *Decoder loss for reducing color shift* (Sec. 4.4). Directly fine-tuning the LDM, via Eq. (1), often leads to color shift, as the supervision is only in the latent space. To address this, we propose a decoder-based reconstruction loss, which provides a supervised loss in the pixel space.

Overview. A visual illustration of our method is provided in Fig. 2. Given a noisy image \mathbf{y} , we use the VAE encoder with residuals to get the condition latent \mathbf{z}_y . This latent is then processed by a context processor, which generates condition features \mathbf{z}_y^l for each layer l . Simultaneously, we sample a noise $\tilde{\mathbf{z}}_T \sim \mathcal{N}(0, \mathbf{I})$ and pass it through the denoising U-Net encoder to extract latent features $\tilde{\mathbf{z}}_t^l$ for each layer. To condition the image features on condition features, we employ a region-based cross-attention module. After iterative processing through the network, the final denoised latent $\tilde{\mathbf{z}}_0$ is input into the residual VAE decoder to provide the final denoised SRGB image $\tilde{\mathbf{x}}_0$.

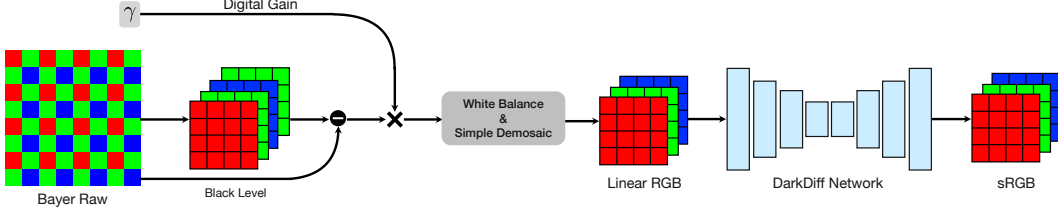


Figure 5: Our data processing pipeline converts Bayer raw input into a linear RGB format by applying white balance and demosaicing to the packed and amplified data. This linear RGB image is then passed to the diffusion model to produce the final sRGB image.

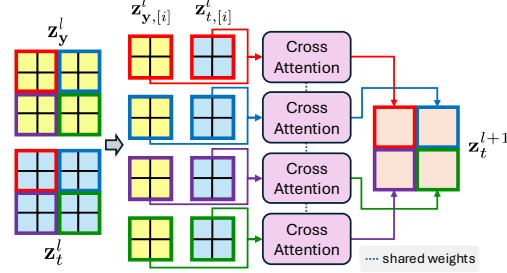


Figure 6: Region-based cross-attention.

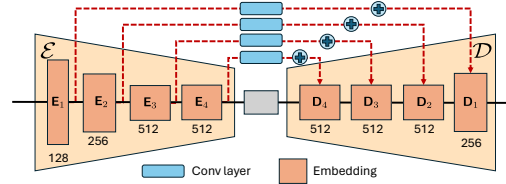


Figure 7: Residual VAE architecture.

4.1 Customized diffusion raw image pipeline

As StableDiffusion was pre-trained on sRGB images and not raw images, we designed this pipeline to reduce this domain gap. Before the enhancement network, we pack Bayer raw data into separate RGBG channels, linearize it by subtracting the black level, and then apply a large digital gain (amplification ratio in SID [5]) to brighten the image. We then apply white balance and simple demosaic such that the data is in brightened linear RGB (LRGB) space. The diffusion model only learns partial ISP processing of denoising and maps the noisy linear RGB images to sRGB images; See Fig. 5. With this design, the noise on the original raw images is evenly amplified and still remains zero mean, which are good properties for the enhancement network to deal with.

4.2 Region-based cross-attention for conditioning

The main drawback of standard cross-attention is that it lacks locality, *i.e.*, all of the tokens are attentive to *all* the spatial locations in the noisy condition image \mathbf{y} . To introduce a sense of locality to cross-attention, we introduce *region-based cross-attention*, which computes attention over a group of localized image patches. See Fig. 6 for illustration.

Formally, the image latent $\mathbf{z}_t \in \mathbb{R}^{H \times W \times d}$ is passed through the encoder of the U-Net, producing the latent feature \mathbf{z}_t^l at each cross-attention layer l . Similarly, the condition latent $\mathbf{z}_y \in \mathbb{R}^{H \times W \times d}$ is processed by the context processor, which has the same architecture as and weights initialized from the U-Net encoder. For each cross-attention layer l , we group these latents into K^l non-overlapping regions. Each region is then converted into a set of N^l tokens.

Let $\{\mathbf{z}_{t,[i]}^l\}_{i=1}^{K^l}$ and $\{\mathbf{z}_{y,[i]}^l\}_{i=1}^{K^l}$ denote the latent and condition region tokens at layer l , where $\mathbf{z}_{t,[i]}^l, \mathbf{z}_{y,[i]}^l \in \mathbb{R}^{N^l \times d}$. The queries, keys, and values for each i -th region are:

$$\begin{aligned} \mathbf{Q}_{[i]}^l &= \mathbf{z}_{t,[i]}^l (\mathbf{W}_Q^l)^\top, \quad \mathbf{K}_{[i]}^l = \mathbf{z}_{y,[i]}^l (\mathbf{W}_K^l)^\top, \\ \mathbf{V}_{[i]}^l &= \mathbf{z}_{y,[i]}^l (\mathbf{W}_V^l)^\top, \end{aligned} \quad (5)$$

where $\mathbf{W}_Q^l, \mathbf{W}_K^l, \mathbf{W}_V^l$ are *shared* across all the regions. The attention weights for the i -th region are computed as:

$$\mathbf{A}_{[i]}^l = \text{Softmax} \left(\mathbf{Q}_{[i]}^l (\mathbf{K}_{[i]}^l)^\top / \sqrt{d_k^l} \right). \quad (6)$$

Table 1: Quantitative results on Sony set of the SID dataset [5], ratio 300 subset.

Methods	PSNR \uparrow	SSIM \uparrow	LPIPS \downarrow
SID	27.22	0.664	0.235
ELD	26.69	0.659	0.225
LED	22.14	0.5200	0.322
LRD	27.13	0.656	0.232
ED	27.74	0.679	0.240
SD Concat	17.33	0.334	0.240
SD ControlNet	16.70	0.304	0.259
DarkDiff	26.78	0.644	0.186

Table 2: Quantitative results on ELD dataset [49], ratio 200 subset.

Methods	PSNR \uparrow	SSIM \uparrow	LPIPS \downarrow
SID	27.14	0.833	0.175
ELD	27.14	0.832	0.159
LED	24.50	0.674	0.210
LRD	29.22	0.832	0.197
ED	28.17	0.863	0.159
SD Concat	21.17	0.334	0.279
SD ControlNet	21.89	0.422	0.234
DarkDiff	27.06	0.837	0.150

Table 3: Quantitative results on LRD dataset [54], -3EV subset. The existing methods with high PSNR/SSIM tend to over-smooth the images and perform worse on the perceptual metric LPIPS.

Methods	PSNR \uparrow	SSIM \uparrow	LPIPS \downarrow
LRD	30.69	0.802	0.155
SD Concat	18.99	0.475	0.179
SD ControlNet	17.83	0.444	0.190
DarkDiff	29.45	0.776	0.103

Finally, the updated latent at layer l is computed by attending to the condition latent:

$$\mathbf{z}_{t,[i]}^{l+1} = \mathbf{A}_{[i]}^l \mathbf{V}_{[i]}^l. \quad (7)$$

By operating at the region level and performing cross-attention over multiple layers, the model learns to focus on local structures from the condition image.

4.3 Content preservation VAE with residuals

To extract the latent features, the conditioning image \mathbf{y} is first processed through an encoder \mathcal{E} before entering the diffusion process. To preserve the visible content of \mathbf{y} , the encoder must be able to capture the relevant information. As illustrated in Fig. 4, simply passing an image through the encoder and then the decoder of a standard VAE architecture leads to noticeable pixel differences in the reconstruction.

To address this issue, we introduce residual connections between the corresponding encoder and decoder blocks within the VAE. Formally, denote the image embedding at each block b of the encoder as \mathbf{E}_b . The embedding is passed through a convolution layer Conv_b such that the channel size of $\text{Conv}_b(\mathbf{E}_b)$ matches the corresponding decoder embedding \mathbf{D}_b . The residual connection for each block b is expressed as: $\mathbf{D}_{b+1} = \mathbf{D}_b + \text{Conv}_b(\mathbf{E}_b)$. This architecture encourages the details from the conditioning image \mathbf{y} to be better preserved across different resolutions, only compressing the necessary information at the VAE’s bottleneck. The VAE architecture is shown in Fig. 7. Empirically, we observe that the proposed architecture significantly improves reconstruction quality.

4.4 Decoder loss for reducing color shift

A standard LDM training with Eq. (1) only provides supervision in the latent space and suffers from the issue of color shift when the input linear RGB image is too noisy. To ensure that the reconstructed image is visually consistent with the clean ground-truth sRGB image \mathbf{x}_0 , we introduce a loss function on the image space by using the decoder. A multi-step approximation requires backpropagation through all unrolled steps, which is computationally expensive. Instead, we construct a “one-step” approximation of the denoised latent following the derivation by Ho et al. [22]:

$$\hat{\mathbf{z}}_0 = \frac{1}{\sqrt{\bar{\alpha}_t}} (\mathbf{z}_t - \sqrt{1 - \bar{\alpha}_t} \hat{\epsilon}_t), \quad (8)$$

where $\bar{\alpha}_t = \prod_{s=1}^t \alpha_s$ and α_t is the noise scheduling factor.

The VAE decoder \mathcal{D} then maps this approximated latent $\hat{\mathbf{z}}_0$ back to the sRGB image space. The image-space reconstruction loss is given by:

$$\mathcal{L}_{\text{image}} = \mathbb{E}_{\mathbf{x}} [\|\mathbf{x} - \mathcal{D}(\hat{\mathbf{z}}_0)\|_2^2]. \quad (9)$$

As the loss in the sRGB space, it will directly penalize the model if there is a color shift.

4.5 Training and implementation details

Training details. We train the proposed model in two stages. We first fine-tune the pre-trained VAE on pairs of noisy linear RGB and clean sRGB images following the loss function proposed by Rombach et al. [39], which is a combination of the perceptual loss [56], a patch-based adversarial loss [10], and a KL divergence regularizing the latent space.

Table 4: Ablation results of the contribution of each component in the model framework.

Components			Metrics		
§4.2	§4.3	§4.4	PSNR	SSIM	LPIPS
✓	✓	✓	26.52	0.642	0.198
✓	✓	✓	22.44	0.566	0.224
✓	✓	✓	26.40	0.642	0.198
✓	✓	✓	26.78	0.644	0.186

Table 5: Ablation on the VAE’s input and output format. The proposed LRGB-sRGB performs the best.

Data	PSNR	SSIM	LPIPS
Raw-Raw	22.17	0.451	0.265
Raw-sRGB	25.34	0.614	0.204
LRGB-sRGB	26.78	0.644	0.186

Table 6: Ablation results of image conditioning modules. All the results here are *using our proposed residual VAE*.

Module	PSNR	SSIM	LPIPS
Concat	26.52	0.644	0.192
ControlNet	26.54	0.642	0.211
Global XAttn	21.00	0.541	0.381
Rb-XAttn	26.78	0.644	0.186

In the second stage, we train the latent diffusion model using the latent representations produced by the fine-tuned VAE. The U-Net’s weights are initialized using the weights from a pre-trained LDM. The training objective is given by $\mathcal{L} = \mathcal{L}_{\text{LDM}} + \lambda \cdot \mathcal{L}_{\text{image}}$, where λ balances between the two loss functions. More implementation details are in the Appendix.

Controlling generation with classifier-free guidance. During inference time, we control the level of generation in DarkDiff by using classifier-free guidance [21] and extending the denoiser to take in an additional input, *i.e.*, $\epsilon_{\theta}(\mathbf{z}_t, \mathbf{c}, t)$. The adjusted noise prediction $\hat{\epsilon}$ is controlled by linearly combining the conditional and unconditional predictions, *i.e.*,

$$\hat{\epsilon} = \epsilon_{\theta}(\tilde{\mathbf{z}}_t, t) + \omega \cdot (\epsilon_{\theta}(\tilde{\mathbf{z}}_t, \mathbf{c}, t) - \epsilon_{\theta}(\tilde{\mathbf{z}}_t, t)), \quad (10)$$

where ϵ is the guidance weight. As shown in Fig. 8, when guidance is one, the model tends to smooth the details of the ground and background with less generation, *e.g.*, on the texture of the cloth. Larger guidance helps the model generate details while also having the potential to introduce artifacts and more hallucinations.

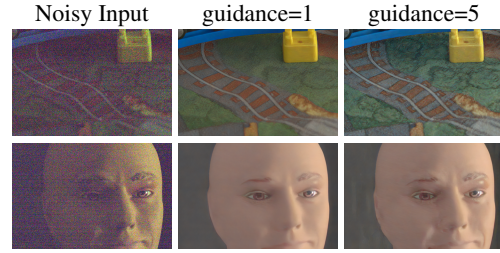


Figure 8: Results of classifier-free guidance at different strengths. A small amount of guidance smooths patterns; strong guidance adds details.

5 Experiments

Datasets. We evaluate our proposed framework on three widely used low-light raw image datasets:

SID [5], ELD [49], and the recently introduced LRD [54]. For the SID dataset, we follow the split used by Wei et al. [49], utilizing the Sony subset and training our models for both SID and ELD evaluations on the 280 image pairs in the SID training set. For the LRD test set, we train the model using the corresponding LRD training set, which contains 1,440 training pairs. Images captured in bright light normally have high SNR values and do not necessarily require content generation. We focus on the most challenging cases: extreme low-light images with high digital gain: $\times 300$ in SID, $\times 200$ in ELD, and -3EV in LRD. For all experiments, we use the real captured paired data for evaluation.

Evaluation metrics. We evaluate the performance of our framework using the Peak Signal-to-Noise Ratio (PSNR), Structural Similarity Index (SSIM), and Learned Perceptual Image Patch Similarity (LPIPS). While PSNR and SSIM are commonly reported metrics, they **do not always correlate well with human perception for generative tasks** [2, 13, 14]; nonetheless, we report them for completeness. For image-to-image tasks, it is more common to use LPIPS to evaluate the generative capability [8, 28, 30]. We illustrate the behavior of these metrics in Fig. 9.

Baselines. We consider the following groups of baselines.

- *Regression-based:* SID [5], ELD [49], LED [27], and LRD [54].

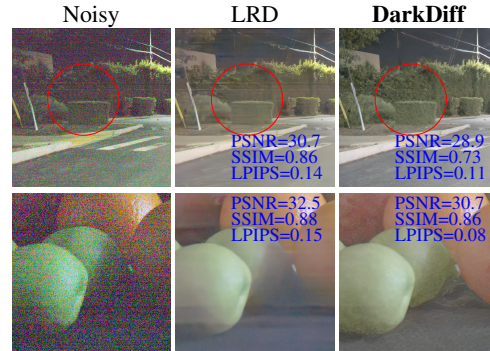


Figure 9: LPIPS better reflects perceptual quality than PSNR or SSIM [56].

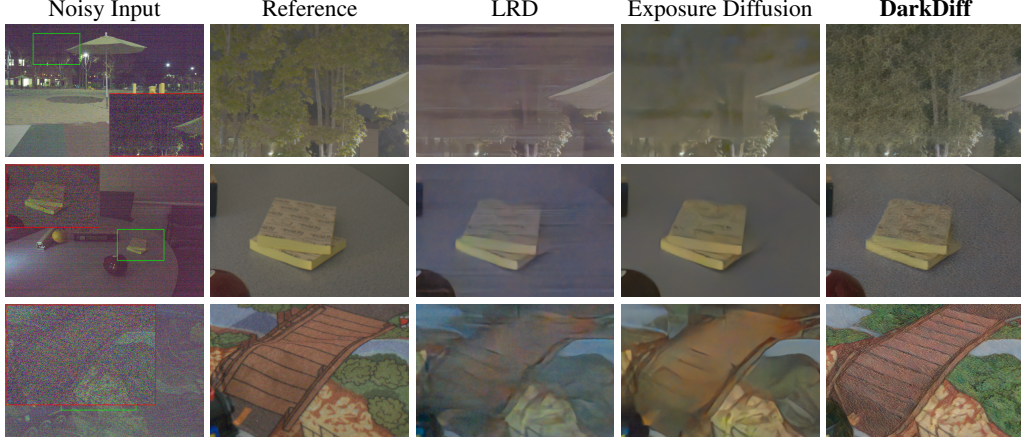


Figure 10: Low-light image denoising results on SID [5]. Our method generates patterns on the trees, the sticky notes, and the bridge. In contrast, the baselines’ results are smoothed out, *e.g.*, the details of the trees are barely visible.

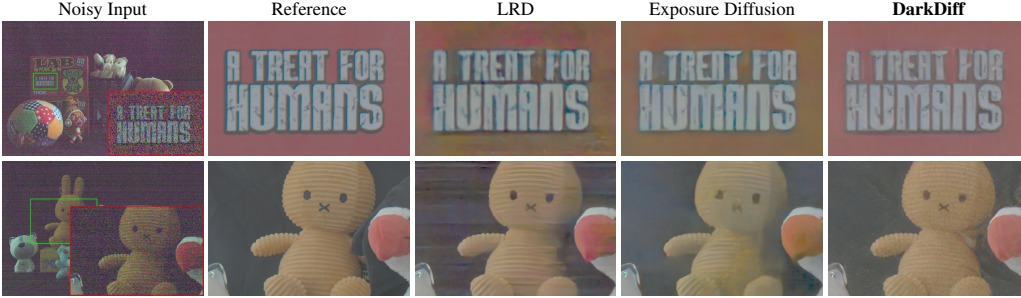


Figure 11: Low-light image denoising results on ELD [49]. Our results maintain the color of the images and have fewer artifacts than the baseline results. Notably, the furry texture of the brown plush is more vivid in our result.

- *Diffusion-based*: ExposureDiffusion (ED) [47], SD Concat, and SD ControlNet. *To the best of our knowledge, ED is the current SOTA on public benchmarks.*

For *SD Concat*, we modified the model by concatenating the noisy latent \mathbf{z}_y as input to the diffusion process. This is inspired by Brooks et al. [4], where they use concat to condition a diffusion model for the task of image editing. *SD ControlNet* is a baseline using ControlNet [55] as the conditioning module. For all methods as well as ground-truth, we use the same ISP process, *i.e.*, rawpy library, for final evaluation in sRGB. See the Appendix for more details.

5.1 Results

Quantitative results. We report the results on SID [5] dataset in Tab. 1. As we can observe, our method achieves the best LPIPS, outperforming the second-best baseline of ELD by 20.9%. Our method remains competitive on PSNR and SSIM. To understand why PSNR and SSIM are not the best metrics for generative tasks, please see comparisons in Fig. 9. Our results have more vivid details like tree leaves and sharper textures of the fruits and cloth when compared to LRD. This higher quality is accurately captured by LPIPS but not reflected in PSNR and SSIM. Notice the line artifacts in LRD, as highlighted in the red circle. These limitations of PSNR and SSIM have also been discussed in prior works on ill-posed image restoration [2, 13, 14].

Next, the results on the ELD [49] and LRD [54] datasets are provided in Tab. 2 and Tab. 3. Similar to the results for SID, we achieve the highest LPIPS while maintaining competitive PSNR and SSIM.

Qualitative results on SID [5] is shown in Fig. 10. We observe that in regions with large noise (extremely dark areas), our method reconstructs realistic details, *e.g.*, trees in the background and texture on sticky notes. In comparison, the state-of-the-art methods failed to recover enough image details in those most challenging cases.

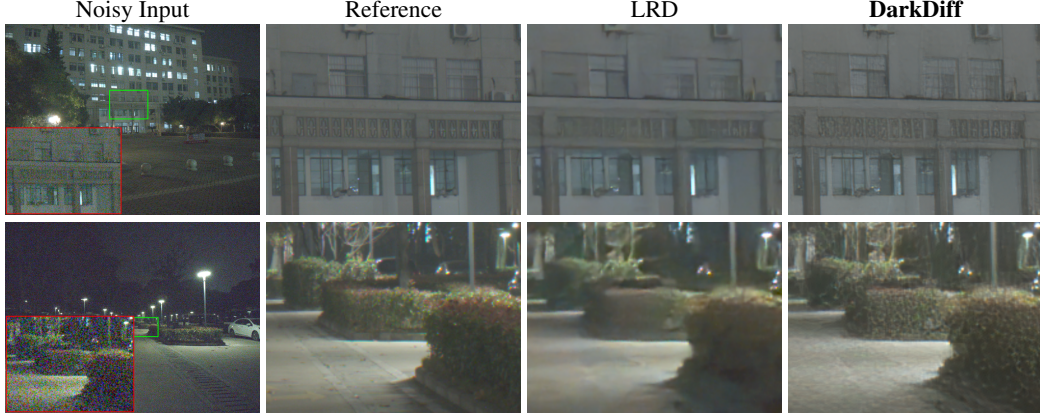


Figure 12: Low-light image denoising results on LRD [54]. Our method generates the details of the building pattern and the textures of the bushes. While the SOTA method, LRD, generates overly smoothed images and lacks details. Best viewed on screens instead of printed.

For the ELD dataset [40], qualitative results are shown in Fig. 11. We observe that the color of the red box is maintained by our method. The SOTA methods contain visible artifacts in those extremely low SNR regions, including color shift, line artifacts, and over-smoothing.

For the LRD dataset [54], despite being captured by a different camera sensor, our method still generalizes well. As shown in Fig. 12, our method consistently generates more detailed images than the state-of-the-art method, avoiding an overly smoothed image. More qualitative results are provided in the appendix.

5.2 Ablation Studies

We conduct ablation studies using the SID dataset [5].

Ablating model components. We investigate the importance of various components introduced by our model, including region-based cross-attention (Sec. 4.2), residual VAE (Sec. 4.3), and decoder-based reconstruction loss. (Sec. 4.4). Here, we replace region-based cross-attention with concatenation in the diffusion input in the first row. As shown in Tab. 4, the performance drops if any components are removed. The result also shows that residual VAE plays a crucial role in the performance gain.

Impact of data format. We evaluate the effect of different input/output data formats on low-light imaging. Since the baseline methods utilize either raw or sRGB formats, we compare our approach with these in Tab. 5 and demonstrate that using linear RGB input aligns more effectively with the pre-trained model’s input spaces while also preserving the information of the raw data.

Ablating conditioning modules. To study the effectiveness of region-based cross attention, we compare it with other alternative conditioning methods, including direct concatenation (Concat), ControlNet, and global cross attention. This ablation is conducted using the proposed residual VAE trained in stage 1, *i.e.*, we are only ablation the conditioning module in stage 2 training. As shown in Tab. 6, the proposed region-based attention mechanism achieves the highest quality, while Concat and ControlNet perform similarly.

6 Conclusion

We proposed a novel approach to enhancing raw images taken in extreme low-light conditions. We retasked the generative capability of a pre-trained diffusion model into Camera ISP by carefully considering which part of the ISP should be replaced with a diffusion model. Our method improves common issues in extreme low-light image enhancement of over-smoothing, local structural fidelity, and color shifts. We propose a region-based cross-attention, a content-preserving VAE, and a decoder-based reconstruction loss to better leverage the diffusion model over the generated content. Experiments on three datasets demonstrate that our approach outperforms SOTA methods in perceptual quality.

References

- [1] Abdelrahman Abdelhamed, Marcus A Brubaker, and Michael S Brown. Noise flow: Noise modeling with conditional normalizing flows. In *Proc. ICCV*, 2019. 2
- [2] Yochai Blau and Tomer Michaeli. The perception-distortion tradeoff. In *Proc. CVPR*, 2018. 7, 8
- [3] Tim Brooks, Ben Mildenhall, Tianfan Xue, Jiawen Chen, Dillon Sharlet, and Jonathan T Barron. Unprocessing images for learned raw denoising. In *Proc. CVPR*, 2019. 2
- [4] Tim Brooks, Aleksander Holynski, and Alexei A Efros. Instructpix2pix: Learning to follow image editing instructions. In *Proc. CVPR*, 2023. 8, 14
- [5] Chen Chen, Qifeng Chen, Jia Xu, and Vladlen Koltun. Learning to see in the dark. In *Proc. CVPR*, 2018. 1, 2, 3, 5, 6, 7, 8, 9, 14, 15, 16, 17
- [6] Chun-Fu Richard Chen, Quanfu Fan, and Rameswar Panda. CrossViT: Cross-attention multi-scale vision transformer for image classification. In *Proc. CVPR*, 2021. 3
- [7] Minghao Chen, Iro Laina, and Andrea Vedaldi. Training-free layout control with cross-attention guidance. In *Proc. WACV*, 2024. 3
- [8] Guillaume Couairon, Jakob Verbeek, Holger Schwenk, and Matthieu Cord. DiffEdit: Diffusion-based semantic image editing with mask guidance. In *Proc. ICLR*, 2023. 7
- [9] Jiachen Dang, Yong Zhong, and Xiaolin Qin. PPformer: Using pixel-wise and patch-wise cross-attention for low-light image enhancement. *Computer Vision and Image Understanding*, 241:103930, 2024. 3
- [10] Patrick Esser, Robin Rombach, and Bjorn Ommer. Taming transformers for high-resolution image synthesis. In *Proc. CVPR*, 2021. 6
- [11] Ben Fei, Zhaoyang Lyu, Liang Pan, Junzhe Zhang, Weidong Yang, Tianyue Luo, Bo Zhang, and Bo Dai. Generative diffusion prior for unified image restoration and enhancement. In *Proc. CVPR*, 2023. 3
- [12] Sicheng Gao, Xuhui Liu, Bohan Zeng, Sheng Xu, Yanjing Li, Xiaoyan Luo, Jianzhuang Liu, Xiantong Zhen, and Baochang Zhang. Implicit diffusion models for continuous super-resolution. In *Proc. CVPR*, 2023. 3
- [13] Jinjin Gu, Haoming Cai, Haoyu Chen, Xiaoxing Ye, Jimmy Ren, and Chao Dong. Pipal: a large-scale image quality assessment dataset for perceptual image restoration. In *Proc. ECCV*, 2020. 7, 8
- [14] Jinjin Gu, Haoming Cai, Chao Dong, Jimmy S. Ren, Radu Timofte, Yuan Gong, Shanshan Lao, and et al Shi, Shuwei. NTIRE 2022 challenge on perceptual image quality assessment. In *Proc. CVPR Workshops*, 2022. 7, 8
- [15] Xiaojie Guo and Qiming Hu. Low-light image enhancement via breaking down the darkness. *IJCV*, 2023. 2
- [16] Xiaojie Guo, Yu Li, and Haibin Ling. Lime: Low-light image enhancement via illumination map estimation. *IEEE TIP*, 2016. 2
- [17] Samuel W Hasinoff, Dillon Sharlet, Ryan Geiss, Andrew Adams, Jonathan T Barron, Florian Kainz, Jiawen Chen, and Marc Levoy. Burst photography for high dynamic range and low-light imaging on mobile cameras. *ACM TOG*, 2016. 1
- [18] Chunming He, Chengyu Fang, Yulun Zhang, Tian Ye, Kai Li, Longxiang Tang, Zhenhua Guo, Xiu Li, and Sina Farsiu. Reti-Diff: Illumination degradation image restoration with retinex-based latent diffusion model. *arXiv preprint arXiv:2311.11638*, 2023. 3
- [19] Chunming He, Yuqi Shen, Chengyu Fang, Fengyang Xiao, Longxiang Tang, Yulun Zhang, Wangmeng Zuo, Zhenhua Guo, and Xiu Li. Diffusion models in low-level vision: A survey. *arXiv preprint arXiv:2406.11138*, 2024. 3
- [20] Amir Hertz, Ron Mokady, Jay Tenenbaum, Kfir Aberman, Yael Pritch, and Daniel Cohen-or. Prompt-to-prompt image editing with cross-attention control. In *Proc. ICLR*, 2023. 3
- [21] Jonathan Ho and Tim Salimans. Classifier-free diffusion guidance. *arXiv preprint arXiv:2207.12598*, 2022. 7
- [22] Jonathan Ho, Ajay Jain, and Pieter Abbeel. Denoising diffusion probabilistic models. 2020. 3, 6

- [23] Jinhui Hou, Zhiyu Zhu, Junhui Hou, Hui Liu, Huanqiang Zeng, and Hui Yuan. Global structure-aware diffusion process for low-light image enhancement. In *Proc. CVPR*, 2024. 3
- [24] Hai Jiang, Ao Luo, Haoqiang Fan, Songchen Han, and Shuaicheng Liu. Low-light image enhancement with wavelet-based diffusion models. *ACM TOG*, 2023.
- [25] Hai Jiang, Ao Luo, Xiaohong Liu, Songchen Han, and Shuaicheng Liu. Lightendiffusion: Unsupervised low-light image enhancement with latent-retinex diffusion models. In *Proc. ECCV*, 2024. 3
- [26] Xin Jin, Linghao Han, Zhen Li, Zhi Chai, Chunle Guo, and Chongyi Li. Dnf: Decouple and feedback network for seeing in the dark. In *Proc. CVPR*, 2023. 3
- [27] Xin Jin, Jia-Wen Xiao, Ling-Hao Han, Chunle Guo, Ruixun Zhang, Xialei Liu, and Chongyi Li. Lighting every darkness in two pairs: A calibration-free pipeline for raw denoising. In *Proc. ICCV*, 2023. 2, 7, 15, 16, 17
- [28] Tero Karras, Samuli Laine, Miika Aittala, Janne Hellsten, Jaakko Lehtinen, and Timo Aila. Analyzing and improving the image quality of stylegan. In *Proc. CVPR*, 2020. 7
- [29] Bahjat Kawar, Michael Elad, Stefano Ermon, and Jiaming Song. Denoising diffusion restoration models. In *Proc. NeurIPS*, 2022. 3
- [30] Bahjat Kawar, Shiran Zada, Oran Lang, Omer Tov, Huiwen Chang, Tali Dekel, Inbar Mosseri, and Michal Irani. Imagic: Text-based real image editing with diffusion models. In *Proc. CVPR*, 2023. 7
- [31] Diederik P Kingma. Adam: A method for stochastic optimization. *arXiv preprint arXiv:1412.6980*, 2014. 13, 14
- [32] Benjamin Lefauveux, Francisco Massa, Diana Liskovich, Wenhan Xiong, Vittorio Caggiano, Sean Naren, Min Xu, Jieru Hu, Marta Tintore, Susan Zhang, Patrick Labatut, Daniel Haziza, Luca Wehrstedt, Jeremy Reizenstein, and Grigory Sizov. xFormers: A modular and hackable transformer modelling library. <https://github.com/facebookresearch/xformers>, 2022. 14
- [33] Orly Liba, Kiran Murthy, Yun-Ta Tsai, Tim Brooks, Tianfan Xue, Nikhil Karnad, Qiurui He, Jonathan T Barron, Dillon Sharlet, Ryan Geiss, et al. Handheld mobile photography in very low light. *ACM TOG*, 2019. 1
- [34] Xinqi Lin, Jingwen He, Ziyang Chen, Zhaoyang Lyu, Ben Fei, Bo Dai, Wanli Ouyang, Yu Qiao, and Chao Dong. DiffBIR: Towards blind image restoration with generative diffusion prior. *arXiv preprint arXiv:2308.15070*, 2023. 3, 14
- [35] Kin Gwn Lore, Adedotun Akintayo, and Soumik Sarkar. Llnet: A deep autoencoder approach to natural low-light image enhancement. *Pattern Recognition*, 2017. 2
- [36] Andreas Lugmayr, Martin Danelljan, Andres Romero, Fisher Yu, Radu Timofte, and Luc Van Gool. Repaint: Inpainting using denoising diffusion probabilistic models. In *Proc. CVPR*, 2022. 3
- [37] Cindy M Nguyen, Eric R Chan, Alexander W Bergman, and Gordon Wetzstein. Diffusion in the dark: A diffusion model for low-light text recognition. In *Proc. WACV*, 2024. 3
- [38] Ozan Özdenizci and Robert Legenstein. Restoring vision in adverse weather conditions with patch-based denoising diffusion models. *IEEE TPAMI*, 2023. 3
- [39] Robin Rombach, Andreas Blattmann, Dominik Lorenz, Patrick Esser, and Björn Ommer. High-resolution image synthesis with latent diffusion models. In *Proc. CVPR*, 2022. 2, 3, 6
- [40] Olaf Ronneberger, Philipp Fischer, and Thomas Brox. U-net: Convolutional networks for biomedical image segmentation. In *Proc. MICCAI*, 2015. 3, 9
- [41] Jascha Sohl-Dickstein, Eric Weiss, Niru Maheswaranathan, and Surya Ganguli. Deep unsupervised learning using nonequilibrium thermodynamics. In *Proc. ICML*, 2015. 3
- [42] Jiaming Song, Chenlin Meng, and Stefano Ermon. Denoising diffusion implicit models. *arXiv preprint arXiv:2010.02502*, 2020. 14
- [43] Yang Song and Stefano Ermon. Generative modeling by estimating gradients of the data distribution. In *Proc. NeurIPS*, 2019. 3
- [44] Yang Song and Stefano Ermon. Improved techniques for training score-based generative models. In *Proc. NeurIPS*, 2020. 3

- [45] Yinhuai Wang, Jiwen Yu, and Jian Zhang. Zero-shot image restoration using denoising diffusion null-space model. *arXiv preprint arXiv:2212.00490*, 2022. 3
- [46] Yinglong Wang, Zhen Liu, Jianzhuang Liu, Songcen Xu, and Shuaicheng Liu. Low-light image enhancement with illumination-aware gamma correction and complete image modelling network. In *Proc. ICCV*, 2023. 2
- [47] Yufei Wang, Yi Yu, Wenhan Yang, Lanqing Guo, Lap-Pui Chau, Alex C Kot, and Bihan Wen. ExposureD-iffusion: Learning to expose for low-light image enhancement. In *Proc. ICCV*, 2023. 1, 2, 3, 8, 15, 16, 17
- [48] Zhouxia Wang, Jiawei Zhang, Runjian Chen, Wenping Wang, and Ping Luo. Restoreformer: High-quality blind face restoration from undegraded key-value pairs. In *Proc. CVPR*, 2022. 3
- [49] Kaixuan Wei, Ying Fu, Jiaolong Yang, and Hua Huang. A physics-based noise formation model for extreme low-light raw denoising. In *Proc. CVPR*, 2020. 2, 3, 6, 7, 8, 14, 15, 16, 17
- [50] Qiang Wen, Yazhou Xing, Zhefan Rao, and Qifeng Chen. LDM-ISP: Enhancing neural isp for low light with latent diffusion models. *arXiv preprint arXiv:2312.01027*, 2023. 3
- [51] Jay Whang, Mauricio Delbracio, Hossein Talebi, Chitwan Saharia, Alexandros G Dimakis, and Peyman Milanfar. Deblurring via stochastic refinement. In *Proc. CVPR*, 2022. 3
- [52] Xiaogang Xu, Ruixing Wang, and Jiangbo Lu. Low-light image enhancement via structure modeling and guidance. In *Proc. CVPR*, 2023. 2
- [53] Xunpeng Yi, Han Xu, Hao Zhang, Linfeng Tang, and Jiayi Ma. Diff-Retinex: Rethinking low-light image enhancement with a generative diffusion model. In *Proc. ICCV*, 2023. 2, 3
- [54] Feng Zhang, Bin Xu, Zhiqiang Li, Xinran Liu, Qingbo Lu, Changxin Gao, and Nong Sang. Towards general low-light raw noise synthesis and modeling. In *Proc. ICCV*, 2023. 2, 3, 6, 7, 8, 9, 14, 15, 16, 17
- [55] Lvmin Zhang, Anyi Rao, and Maneesh Agrawala. Adding conditional control to text-to-image diffusion models. In *Proc. ICCV*, 2023. 8, 14
- [56] Richard Zhang, Phillip Isola, Alexei A Efros, Eli Shechtman, and Oliver Wang. The unreasonable effectiveness of deep features as a perceptual metric. In *Proc. CVPR*, 2018. 2, 6, 7

Appendix

The appendix is organized as follows:

- In Sec. A1, we provide additional qualitative results. Please also see the attached supplementary material for more comparisons.
- In Sec. A2, we provide additional experimental details in training, inference, and baselines.
- In Sec. A3, we illustrate the limitations of our method.

A1 Additional qualitative results.

We provide more visual results in this section. Specifically, we show the results compared with more baselines listed in Tab. 1. In Fig. A2 and Fig. A3, we provide our indoor results and six baselines. As we can observe, only our results reconstruct the pattern of the book in Fig. A2. The baselines either have color shifts or make the book pattern blurry. In Fig. A3, we reconstruct the heavily noised rail while the baselines blur the rail. In Fig. A4, Fig. A5 and Fig. A6, we show different outdoor scenes, including trees and grass. The baselines overly smoothed the images and lacked details. For example, in Fig. A4, our result generates the leaves of the tree that resemble the reference image, while SD concat generates unrelated details, and the rest baselines simply smooth out the leaves. We provide the qualitative results in full images in the supplementary attachments.

A2 Implementation details

Hyperparameters. For stage 1, we train for 3,000 epochs with a learning rate of $4e^{-5}$. For stage 2, we train 3,000 epochs with a learning rate of $2.5e^{-4}$ for the weights of the context processor and region-based cross-attention and $5e^{-5}$ for the rest of the weights. As we leverage classifier-free guidance in inference time, we randomly replace 5% low-light noisy embeddings with pure Gaussian noise during stage-2 training. During training, we use image crops of size 1200×1200 images. We run inference on the full image.

Model architecture. We use pre-trained Stable Diffusion V2-1 across all the experiments. Here we illustrate the architecture of the proposed path-wise cross-attention modules (Sec. 4.2) and residual VAE (Sec. 4.3). For the region-based cross-attention layer, we keep the architecture and module sizes of the pre-trained Stable Diffusion unchanged and overwrite the forward function of the SpatialTransformer module to make it adapt to small patches instead of the whole input image embedding. For the Residual VAE, to match the shapes between the corresponding encoder and decoder features, we introduce Conv. layers in each block. The architecture details of the added layers are shown in Tab. A1.

Data preprocessing pipeline. The raw input and target images are loaded and packed from the Bayer format into a 4-channel representation. The packing function extracts the RGB channels and normalizes the image using black and white levels. The pipeline for processing input raw Bayer images starts with a preprocessing step where white balance is applied to the raw RGBG data, followed by averaging the two green channels to produce the Linear RGB format. For the target images, the images are converted from raw to sRGB. The pipeline for converting raw Bayer images to sRGB images involves several key processing steps: white balance, binning, color correction, and gamma compression. First, white balance is applied by adjusting the pixel values based on pre-defined gains, ensuring accurate colors under varying lighting conditions. Then, the Bayer image undergoes binning, where the green channels are averaged and combined with the red and blue channels to form a linear RGB image. Color correction is performed by applying a color correction matrix that transforms the image into a more accurate color space. The image is then gamma-compressed to convert it from linear space to a gamma-corrected space, which adjusts the brightness and contrast for display devices.

Stage 1 training. In stage 1, we fine-tune the residual VAE with the paired noisy IRGB and clean sRGB images. Specifically, we add residual connections between the embedding after each encoder block and the embedding before the corresponding decoder block, as illustrated in Fig. 7. We then fine-tune the whole pre-trained VAE as well as the residual connections with Adam [31] for 3,000

Table A1: Convolutional Layers in Residual VAE

Layer	Type	Kernel Size	Stride	Padding	In Channels	Out Channels
1	Conv2d	3×3	1	1	128	256
2	Conv2d	3×3	1	1	256	512
3	Conv2d	3×3	1	1	512	512
4	Conv2d	3×3	1	1	512	512

epochs on both SID [5] and LRD [54] where the learning rate is $4e^{-5}$ and the $\beta_1 = 0.5, \beta_2 = 0.9$. The training is conducted on $8 \times$ A100 GPUS with 80GB memory.

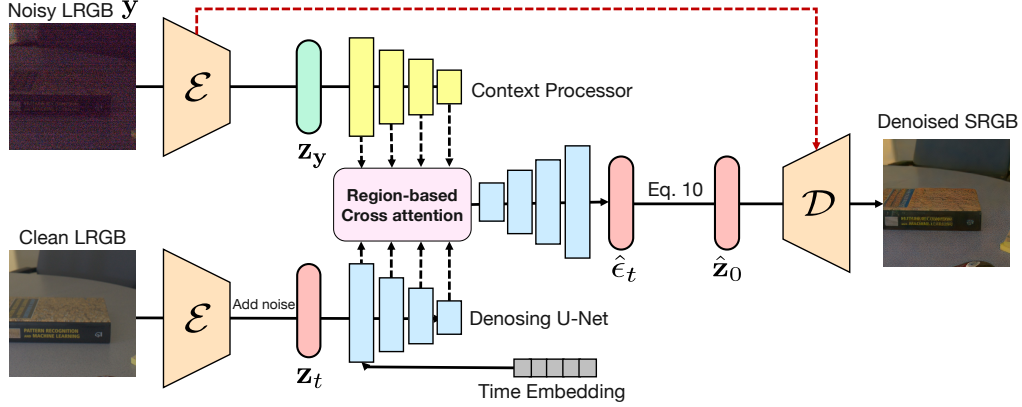


Figure A1: Training pipeline of Stage 2. We input noisy and clean linear RGB images into the same encoder to get \mathbf{z}_y and \mathbf{z}_t . The denoising U-Net outputs the estimated score \hat{e}_t , which is further transferred to $\hat{\mathbf{z}}_0$ based on Eq. (8), then the denoised output is used for computing the decoder-based reconstruction loss.

Stage 2 training. In stage 2, we fine-tune the denoising network to incorporate the generative power of the pre-trained diffusion model. As shown in Fig. A1, both the noisy and clean linear RGB images are input into the same trained VAE encoder from stage 1 to obtain \mathbf{z}_y and \mathbf{z}_t , where the context processor processes \mathbf{z}_y and \mathbf{z}_t is processed by the U-Net encoder. The output of the denoising U-Net is transferred to $\hat{\mathbf{z}}_0$ and decoded by the trained VAE decoder from stage 1. The denoised sRGB output from the decoder is used to compute the decoder-based reconstruction loss defined in Eq. (9). In our experiment, we replace the original cross-attention layers at each block of the original StableDiffusion, which are the layers across image and text embeddings, while we keep the cross-attention layers in the U-Net decoder and use the empty string as the text encoder input. Note that we use Xformers [32] for all the attention modules. We fine-tune the whole U-Net, the context processor, and the region-based cross-attention layers with Adam [31] for 3,000 epochs. The training is conducted on $8 \times$ A100 GPUS with 80GB memory.

Inference. At inference time, we use DDIM [42] with 50 steps for sampling. As both SID[5] and ELD[49] datasets use a Sony A7S camera, we use the model trained on paired images from SID to do inference in ELD. The guidance weights is set to 2.0 for the SID [5] and LRD datasets [5], and 2.5 for ELD datasets [49], respectively.

Baselines. We illustrate the details of the baselines we introduced: SD Concat [4] and SD Control [34, 55]. In SD Concat, we concat \mathbf{z}_y and \mathbf{z}_t in the channel dimension and initialize corresponding weights for the additional channels in the first layer of the U-Net. In SD Control, we follow the structure of the ControlNet [55] that is a copy of the U-Net encoder and takes in the concatenation of \mathbf{z}_y and \mathbf{z}_t [34]. The features from each layer are connected to the features of the corresponding U-Net decoder by using zero-conv layers.

A3 Limitations

The generation ability of the proposed method is constrained by that of the pre-trained diffusion model. We found that the current model has limited strength in enhancing non-English text in low-

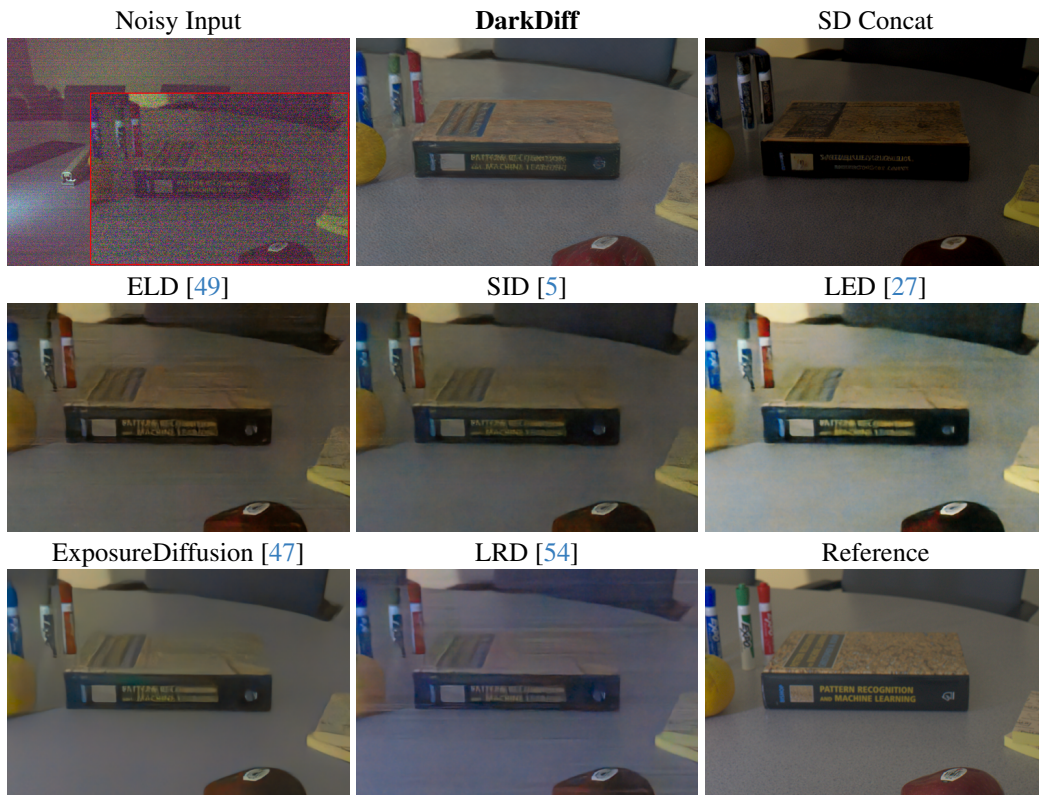


Figure A2: More qualitative results on SID dataset compared with baselines.

light images. In addition, diffusion models usually take much longer inference time than efficient convolutional networks. The proposed approach may need to run on cloud computing instead of on battery-limited devices for practical ISP processing.

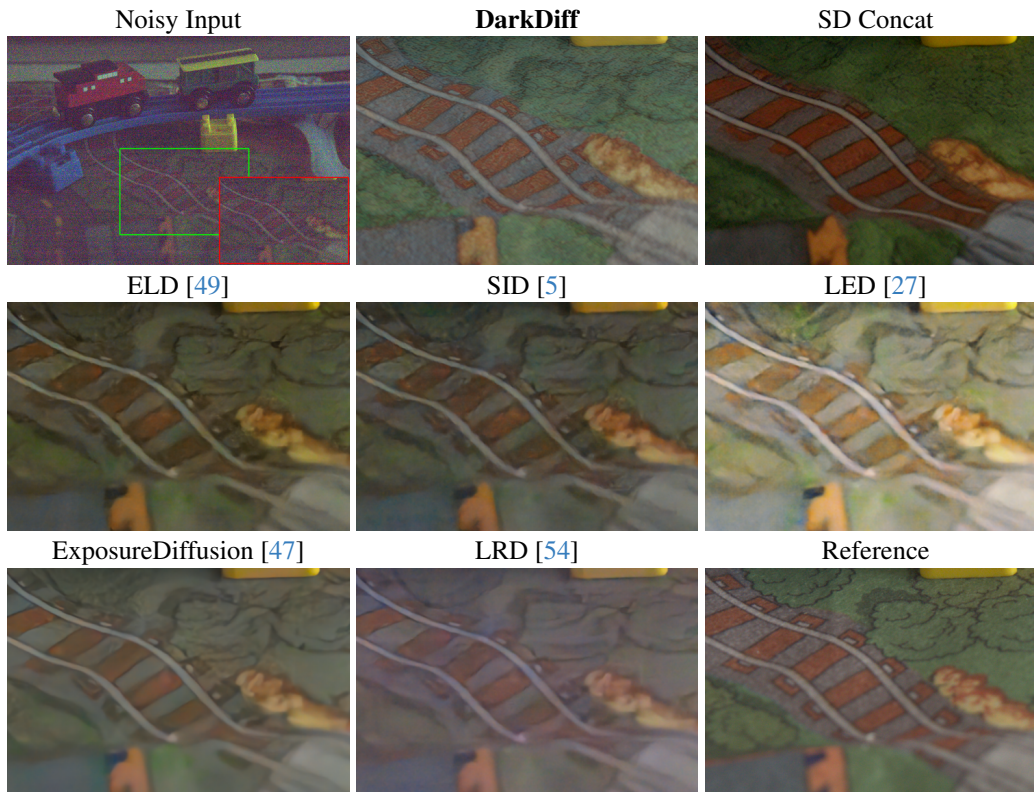


Figure A3: More qualitative results on the SID dataset compared with baselines.

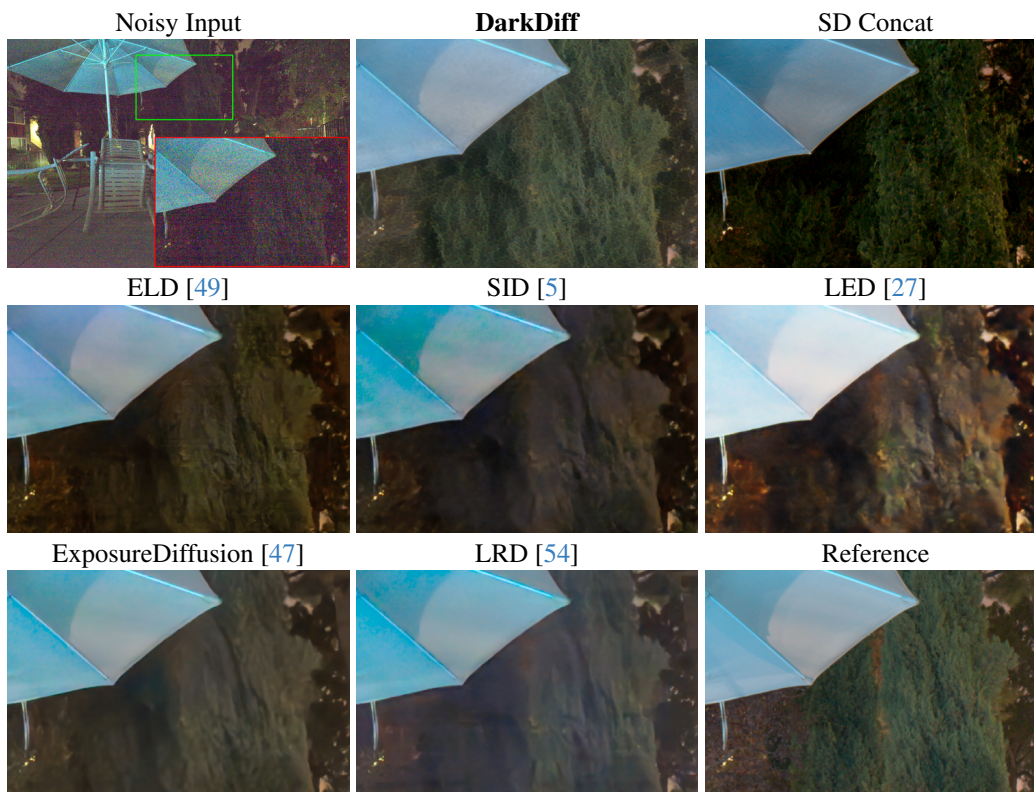


Figure A4: More qualitative results on the SID dataset compared with baselines.

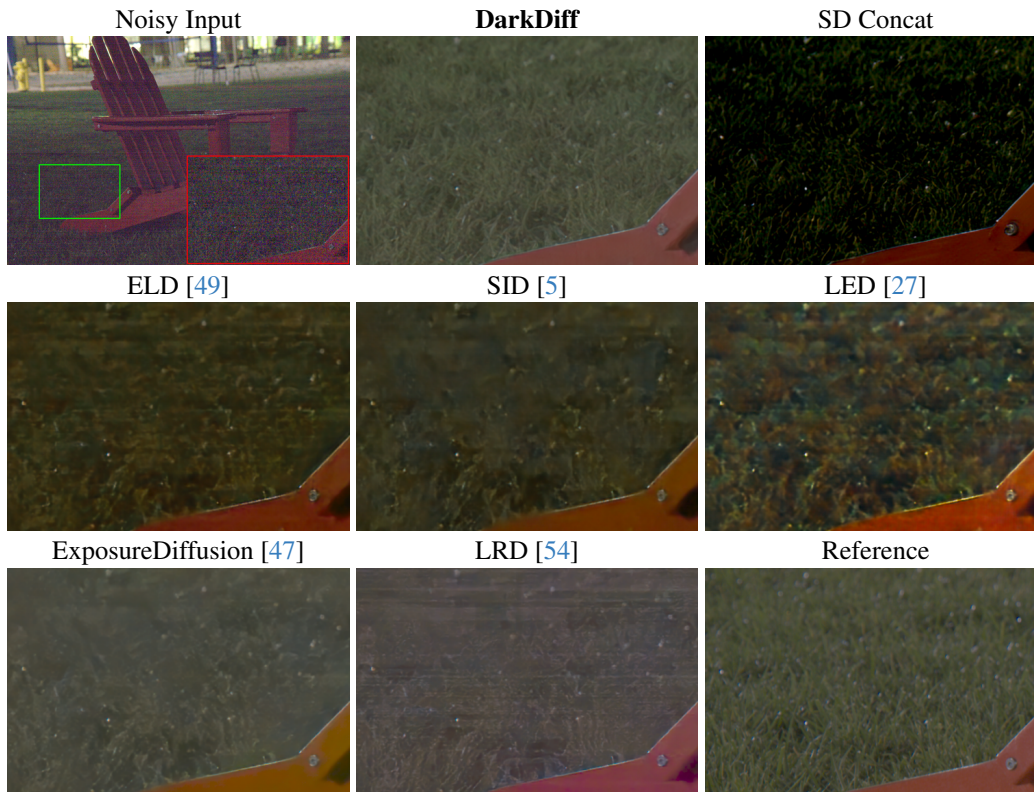


Figure A5: More qualitative results on the SID dataset compared with baselines.

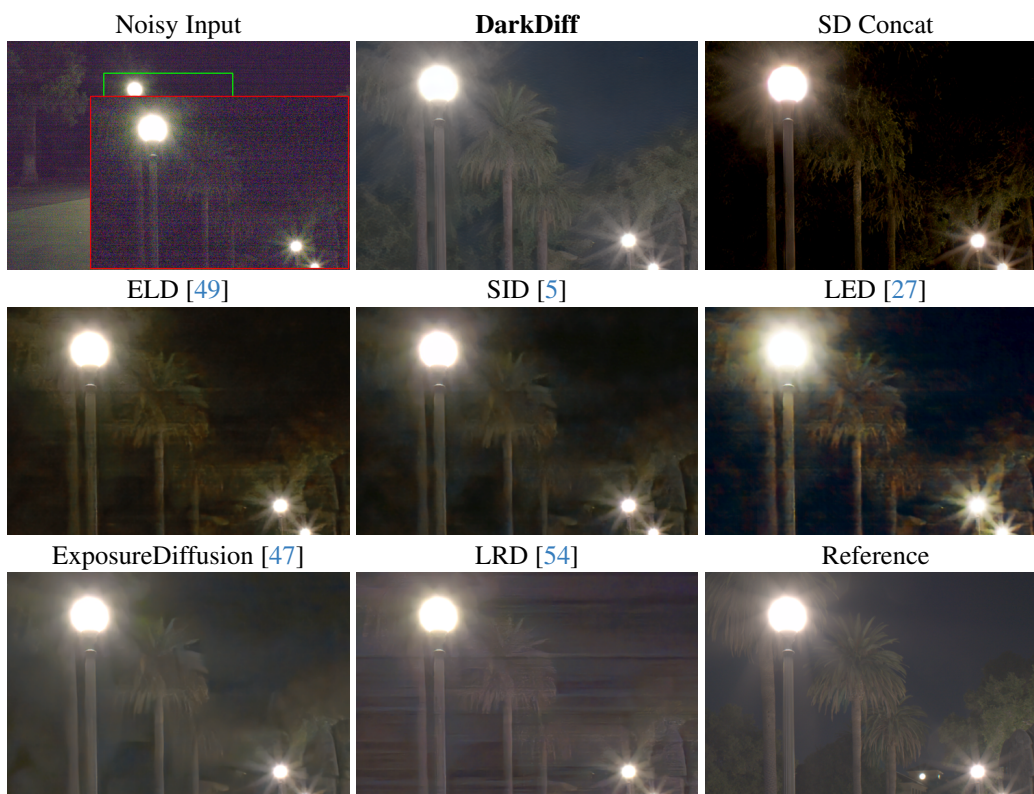


Figure A6: More qualitative results on the SID dataset compared with baselines.